

The Free-Energy Landscape of Clusters of Attractive Hard Spheres

Guangnan Meng,¹ Natalie Arkus,² Michael P. Brenner,² Vinothan N. Manoharan^{1,2*}

The study of clusters has provided a tangible link between local geometry and bulk condensed matter, but experiments have not yet systematically explored the thermodynamics of the smallest clusters. Here we present experimental measurements of the structures and free energies of colloidal clusters in which the particles act as hard spheres with short-range attractions. We found that highly symmetric clusters are strongly suppressed by rotational entropy, whereas the most stable clusters have anharmonic vibrational modes or extra bonds. Many of these clusters are subsets of close-packed lattices. As the number of particles increases from 6 to 10, we observe the emergence of a complex free-energy landscape with a small number of ground states and many local minima.

An isolated system of 10 interacting atoms or molecules will generally adopt a structure that differs in symmetry and average energy from that of a bulk liquid, solid, or even a system containing 100 particles. Yet the study of such small clusters has shed light on a wide variety of phenomena that are observed in the fields of condensed-matter physics and physical chemistry. Since Frank first predicted (1) that icosahedral short-range order would be a hallmark of liquid structure, the study of small-cluster geometry has provided key insights into the frustration underlying nonequilibrium phenomena such as nucleation and the glass transition (2–4). Experimental studies (5, 6) have confirmed this approach through the discovery of local cluster-like order in bulk liquids and glasses, with recent results (7) suggesting that structural arrest in condensed phases may be related to geometrical constraints at the scale of a few particles.

There remain many unresolved questions about cluster geometry and its connection to bulk behavior. Although experiments and simulations have determined the minimum potential-energy clusters for various interactions (8–10), the likelihood of observing a particular cluster structure depends on its free energy (11, 12). What cluster structures are favored by entropy? How does the competition between potential energy and entropy evolve as the number of particles N approaches the bulk limit? Experiments on atomic clusters have not systematically explored these questions; they are limited by short cluster lifetimes, non-equilibrium conditions, and the difficulties of obtaining real-space structures of individual clusters in free space (13).

Here we report experimental results for the structures and free energies of small equilibrium clusters as a function of N , with $N \leq 10$. The experimental system is described in Fig. 1. We use colloidal particles rather than atoms, because

we can precisely control the interactions and directly observe the three-dimensional (3D) structures of the clusters using optical microscopy. To a good approximation, our particles act as “sticky” hard spheres, arguably the simplest nontrivial interaction that leads to clustering. The attraction arises from a depletion interaction with a range of about 1.05 times the particle diameter and a depth of about $4k_B T$, where k_B is Boltzmann’s constant and T is temperature. Because the pair potential is short-ranged, the total potential energy U of a given structure is well approximated by $U = CU_m$, where C is the number of contacts or depletion bonds and U_m is the depth of the pair potential (14). Although these particles form a gel

in bulk, the range and depth of the interaction are consistent with an equilibrium phase diagram showing a fluid-to-crystal transition (15).

We created clusters by isolating small numbers of polystyrene (PS) microspheres in cylindrical microwells filled with water and poly(*N*-isopropylacrylamide) (polyNIPAM) nanoparticles, which cause the depletion interaction. We chemically functionalized the microwells so that particles could not stick to the surfaces. This allows 3D clusters to form in the middle of the wells, unaffected by the boundaries. After the clusters reached equilibrium, we used optical microscopy to observe the cluster structures, and we collected statistics by scanning through the microwell plate, which contains thousands of isolated clusters. Although the number of particles per well is not controlled, we generated enough clusters at each value of $N \leq 10$ to measure their occurrence frequencies. We then determined the free energies from the ensemble statistics through the Boltzmann distribution, $\Delta F = -k_B T \ln P$, where P is the probability of observing a given cluster.

We classified our clusters by comparing them to finite sphere packings. A previous theoretical study (16) enumerated the mechanically stable clusters of idealized hard spheres with infinitesimally short-ranged interactions, revealing the minima of the potential-energy landscape as a function of N . All of the minima at each value of $N \leq 9$ have the same potential energy, which is a result not observed with longer-ranged potentials (17). We explored the structures and proba-

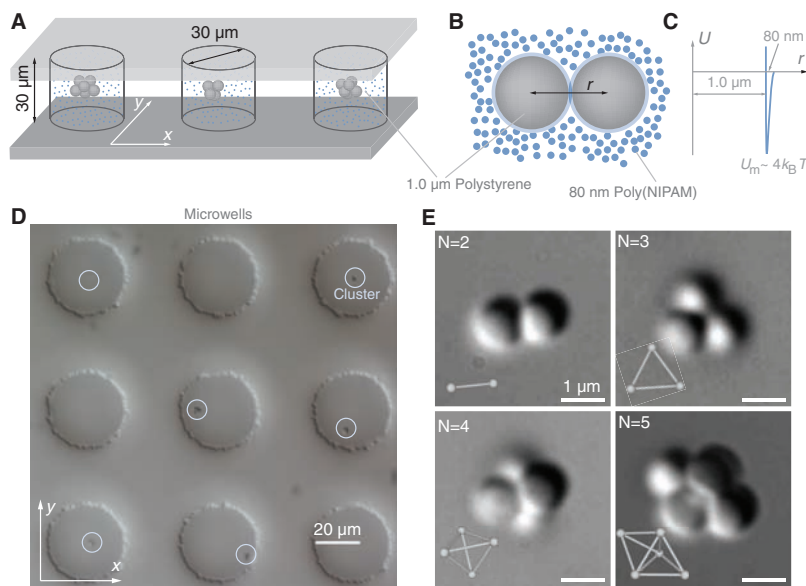


Fig. 1. (A) Diagram of experimental system (14). We used lithography to make microwells with depth and diameter of 30 μm (see also fig. S1). These are filled with a suspension of 1.0- μm -diameter PS spheres and 80-nm polyNIPAM microgel particles, which induce a depletion attraction as illustrated in (B). The number of PS particles per well varies, but the average is about 10. (C) Pair potential as estimated from the Vrij approximation to the Asakura-Oosawa potential (28, 29). Because the range of the depletion attraction is less than 1/10 of the PS sphere diameter, the interaction is strictly pairwise additive. (D) Optical micrograph of microwells with assembled colloidal clusters suspended inside. The circles highlight individual clusters in different microwells. There are about 10^4 microwells per slide. Scale bar, 20 μm . (E) High-magnification optical micrographs of colloidal clusters in microwells with $N = 2, 3, 4$, and 5 particles. These are the only structures that form for $N \leq 5$. Scale bar, 1 μm .

¹Department of Physics, Harvard University, Cambridge, MA 02138, USA. ²Harvard School of Engineering and Applied Sciences, Harvard University, Cambridge, MA 02138, USA.

*To whom correspondence should be addressed. E-mail: vnm@seas.harvard.edu

bilities of these packings at finite temperature, which allows us to map the free-energy landscape (18, 19, 11). All of the observed cluster structures agree with the theoretical predictions. For example, for $N < 6$, we observed one unique structure for each N : a dimer for $N = 2$, trimer for $N = 3$, tetrahedron for $N = 4$, and triangular dipyramid for $N = 5$. The optical micrographs in Fig. 1 show the structures of the smallest clusters.

The first interesting case is $N = 6$. We observed two structures (Fig. 2 and fig. S2), both with $C = 12$ contacts and therefore equivalent potential energy. The first is the octahedron, a Platonic solid. The second, we call a “polytetrahedron.” It consists of a triangular dipyramid with a third tetrahedron added to one of the faces. We observed transitions between the two states on time scales of minutes, indicating that the system is at equilibrium (movie S1).

Although these two structures have the same potential energies, the polytetrahedron occurs about 20 times more often than the octahedron, implying a free-energy difference of about $3k_B T$. This difference can be attributed only to entropy. As shown in Fig. 2, the measured probabilities for the two structures agree well with theoretical calculations based on standard approximations for the rotational and vibrational entropies in the classical limit (14).

The rotational entropy makes the largest contribution to the free-energy difference between the two structures (fig. S2). The rotational partition function is related to two geometrical quantities: the number of orientations, which is proportional to the moment of inertia, and the rotational symmetry of the cluster, or, alternatively, the number of ways one can assemble the same cluster by permuting particle labels (20). Formally, the ratio of the permutational degeneracies of two clusters is inversely proportional to the ratio of their symmetry numbers (21). This permutational degeneracy accounts for a factor of 12 in the polytetrahedron:octahedron probability ratio. The remaining factor of 2 comes from the differences in the moments of inertia and the vibrational entropies.

This result illustrates a general rule for clusters with short-range attractions: among clusters with the same potential energy, highly symmetric structures are extremely unfavorable at equilibrium. By contrast, for the longer-ranged Lennard-Jones 6-12 potential, the octahedron has lower potential energy than the polytetrahedron does (17), so that the dominant structure depends on temperature. The dominance of the polytetrahedron in our system may have consequences for nucleation; the equilibrium phase of attractive hard spheres is a face-centered cubic (FCC) crystal (15), which contains octahedral, not polytetrahedral, subunits.

At $N = 7$, the first chiral structures arise. We observed six cluster structures, two of which are chiral enantiomers. The experimental measurements agree well with the theoretical values for the probabilities of each structure (Fig. 2). For

these small clusters, the most pronounced influence on the probabilities comes from symmetry. At $N = 8$, 3 of the 16 different possible sphere packings never occur in the experiments. These three structures have the highest symmetry numbers, $\sigma = 4, 6$, and 12.

A few structures differ by such small changes in particle spacing that we cannot differentiate between them using our microscope. All of these are variants of pentagonal dipyramids. In a pentagonal dipyramid of seven spheres, the top and bottom spheres of the pyramid are separated by a small gap of $\approx 0.05d$, where d is the sphere diameter. If these two spheres are brought together, a gap of $\approx 0.09d$ opens between two of the

spheres on the pentagon. Because we cannot resolve this gap in our experiments, we have binned these structures together at both $N = 7$ and $N = 8$. The one statistically significant discrepancy between experiment and theory occurs at $N = 8$; it arises because the experimental potential has a range that is comparable to the gap distance. Although we account for this extra potential energy in the probability calculations, the probabilities are sensitive to the magnitude of the potential at the gap distance. If the interaction energy differs from our estimated value by only $0.1k_B T$ in the gap, the theoretical calculation falls within error of the experimental value. This difference could be due to polydispersity in either the depletant

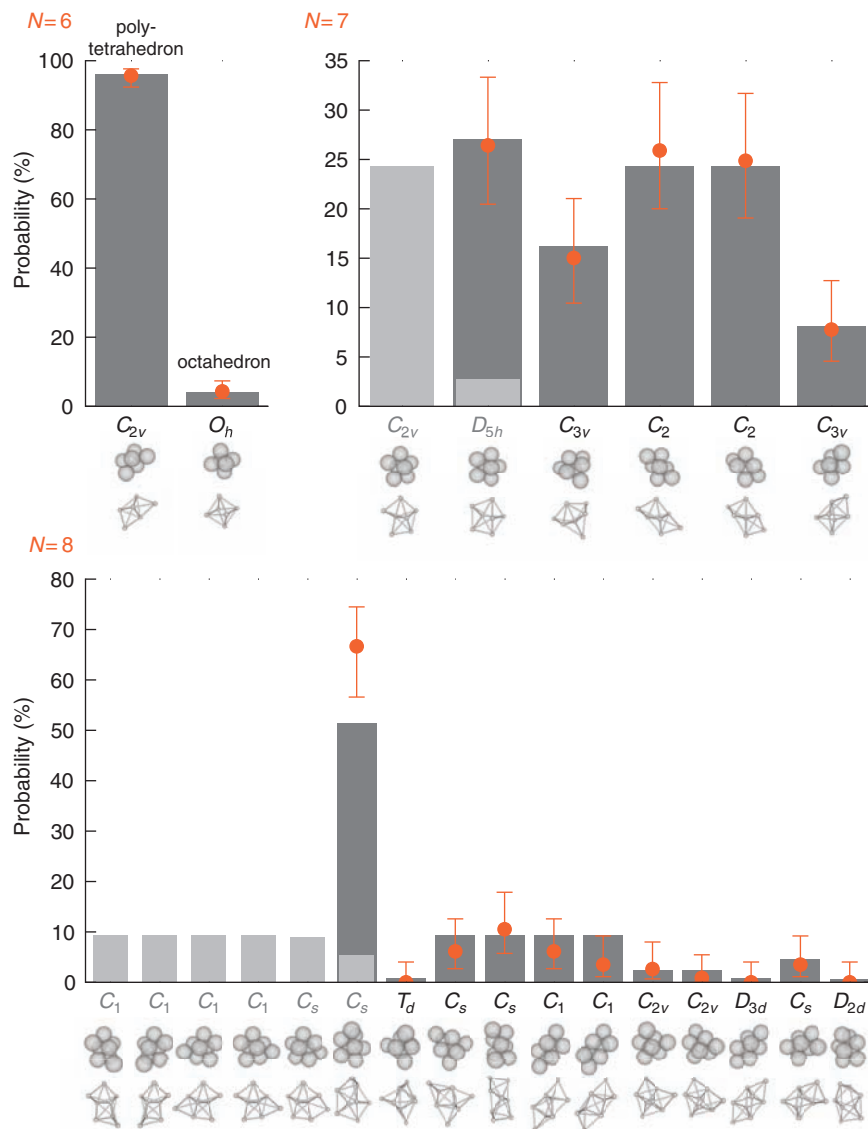


Fig. 2. Comparison of experimental and theoretical (14) cluster probabilities P at $N = 6, 7$, and 8 . Structures that are difficult to differentiate experimentally have been binned together at $N = 7$ and 8 to compare to theory. The calculated probabilities for the individual states are shown as light gray bars, and binned probabilities are dark gray. Orange dots indicate the experimental measurements, with 95% confidence intervals given by the error bars (14) (table S1). Renderings and point groups in Schönflies notation are shown for each structure. The number in the subscript of each symbol indicates the order of the highest rotational symmetry axis, and the letter indicates the symmetry group. The highest symmetry structures are those in D , T , and O groups. Structures in C_1 and C_2 groups occur in chiral pairs.

or large spheres or to another interaction such as van der Waals forces.

The probability distributions in Fig. 2 are “field guides” to the free-energy landscapes at $N = 6, 7$, and 8 . Each structure represents a local free-energy minimum, the depth of which is proportional to the probability. We note two topographical features besides the trend toward structures with low symmetry: first, the number of local minima increases dramatically with N ; and second, the landscape is relatively flat for $N = 7$ and 8 . In other words, there are many shallow minima, but no one minimum has a free energy much larger than any other.

The landscape undergoes a qualitative change for $N \geq 9$. Theoretically we expect some $\Omega = 77$ structures at $N = 9$ and $\Omega = 393$ at $N = 10$, too many to catalog experimentally. We therefore measured only a subset of structures identified by our theoretical study (16). The subset we choose consists of clusters that fall into either of two categories: nonrigid structures, in which one of the vibrational modes is a large-amplitude, anharmonic shear mode; and structures with more than $3N - 6$ bonds. Nonrigidity arises when a cluster contains half-octahedra that share at least one vertex, allowing the cluster to twist over a finite distance without breaking or forming another bond. We expect these packings to have high vibrational entropy. Structures with more than $3N - 6$ bonds can occur for $N \geq 10$. These are the expected ground states.

Indeed, these special packings do occur with high frequency (Fig. 3 and table S2). Because most clusters at $N = 9$ and 10 have equal potential energy, low symmetry, and therefore comparable rotational entropy, we expect the average probability of any one structure in a set of Ω possible clusters to be of order $1/\Omega$. At $N = 9$, we expect an average probability of about 1%, and at $N = 10$, about 0.25%.

By contrast, the one nonrigid structure at $N = 9$ occurs with $P \approx 10\%$. By using the theoretical Ω and the experimental P , we estimate that the free energy of the nonrigid structure is about $2k_B T$ lower than that of an average structure at $N = 9$ (14). Thus the structure is highly stable by nearly half the free energy of an extra bond. The stabilization comes from the vibrational entropy associated with the nonrigid mode (movie S3). Our theoretical calculations (14) predict $P \approx 3\%$, which is lower than the observed probability but higher than all other clusters at $N = 9$. The discrepancy is due to the sensitive dependence of the vibrational partition function on the curvature of the pair potential near the minimum, a consequence of the nonrigid mode. A more precise calculation requires an accurate measurement of electrostatic effects in the experimental pair potential near the depletion well.

At $N = 10$, only 3 of the 393 theoretically possible clusters have $3N - 5 = 25$ contacts, yet these occur about 10% of the time. Although we have only limited statistics for higher N , we con-

tinue to observe the prevalence of a few packings with $3N - 5$ or more bonds. The structures with extra bonds have combined probabilities of 20 to 30% at $N = 11$ and 12 (table S2). Again these probabilities are large compared to $1/\Omega$, even though, in several cases, the clusters have high symmetry. The potential-energy gain is therefore large enough to overcome the deficiency in rotational entropy.

Perhaps the most striking feature of these clusters is that many are subsets of lattice packings, and in particular of the hexagonally close packed (HCP) lattice. The lattice packings are marked in Fig. 3. The underlying reason appears to be that both nonrigidity and extra bonds require the clusters to have octahedral subunits. The propensity for icosahedra (8, 22) in longer-range systems is absent in ours. We observed no icosahedra at either $N = 12$ or 13 , presumably because neither 12-sphere or 13-sphere icosahedra are special clusters for short-range interactions; neither are nonrigid, neither have more than $3N - 6$ bonds, and both have very high symmetry numbers ($\sigma = 60$).

By using the same statistical mechanical approximations that were used to estimate probabilities for $N \leq 8$, we can calculate the free energies of all mechanically stable sphere packings that have been enumerated (16) up to $N = 10$. This yields the free-energy landscape shown in Fig. 4. We see that, in general, the locus of states is correlated with the rotational entropy, which is proportional to $k_B \ln(\sqrt{I}/\sigma)$, where I is the moment of inertia. The only states that lie below this locus occur at $N = 9$ and 10 . These correspond to either nonrigid structures or structures with extra bonds, both of which appear as deeper minima.

The diagram also reveals some new features. First, low-symmetry polytetrahedral states proliferate as N increases. At $N = 10$, where clusters with extra bonds first appear, the absolute probability of observing these ground states is low because of the large number of low-symmetry states that lie at slightly higher free energy.

Second, the highest free-energy structures for $N = 6$ to 10 are convex deltahedra (23), polyhedra with a long history in the field of condensed-matter physics (24, 3). These are not always the most symmetric structures; at $N = 8$ the highest free-energy state is the deltahedron, a snub disphenoid that has lower symmetry than an eight-sphere tetrahedral cluster. The convex deltahedra also happen to be the same “minimal-moment” structures that are formed in capillary-driven assembly of colloidal particles (25). The optimal packings under these nonequilibrium conditions therefore correspond to the least-optimal packings at equilibrium.

Our results suggest that nucleation barriers and structural motifs in attractive hard-sphere systems such as colloidal suspensions will be different from those in systems with longer-range potentials, which tend to favor symmetric structures at sufficiently low temperatures. For $N < 9$, all of our clusters have nearly equivalent potential

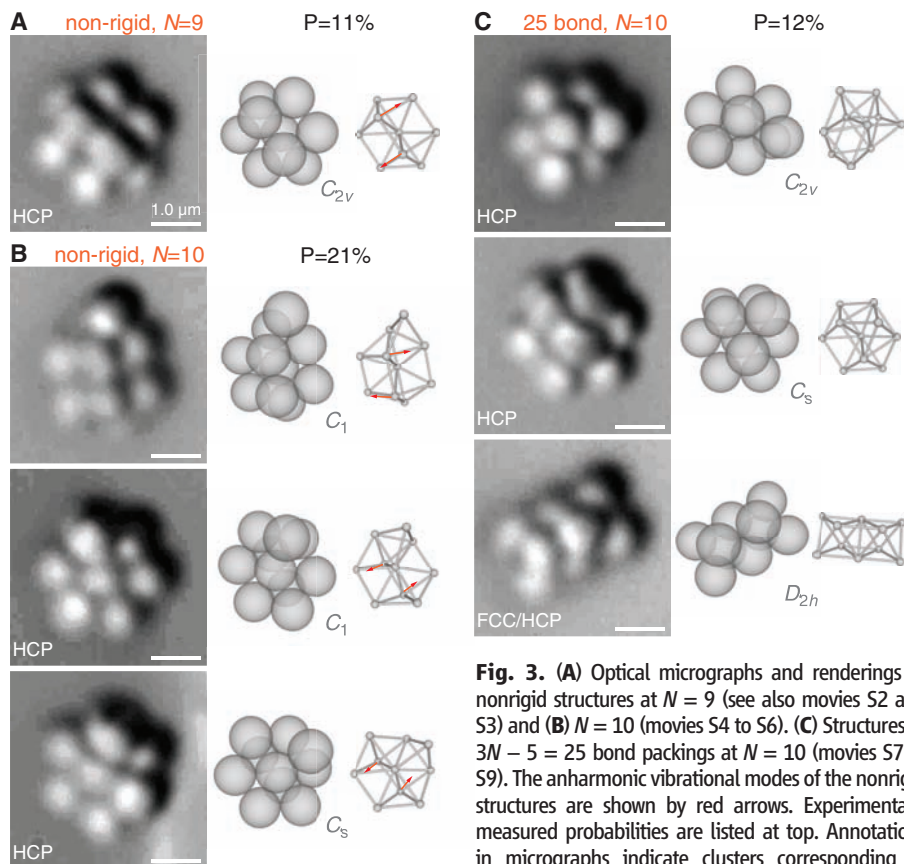


Fig. 3. (A) Optical micrographs and renderings of nonrigid structures at $N = 9$ (see also movies S2 and S3) and (B) $N = 10$ (movies S4 to S6). (C) Structures of $3N - 5 = 25$ bond packings at $N = 10$ (movies S7 to S9). The anharmonic vibrational modes of the nonrigid structures are shown by red arrows. Experimentally measured probabilities are listed at top. Annotations in micrographs indicate clusters corresponding to subsets of HCP or FCC lattices. Scale bars, 1 μm .

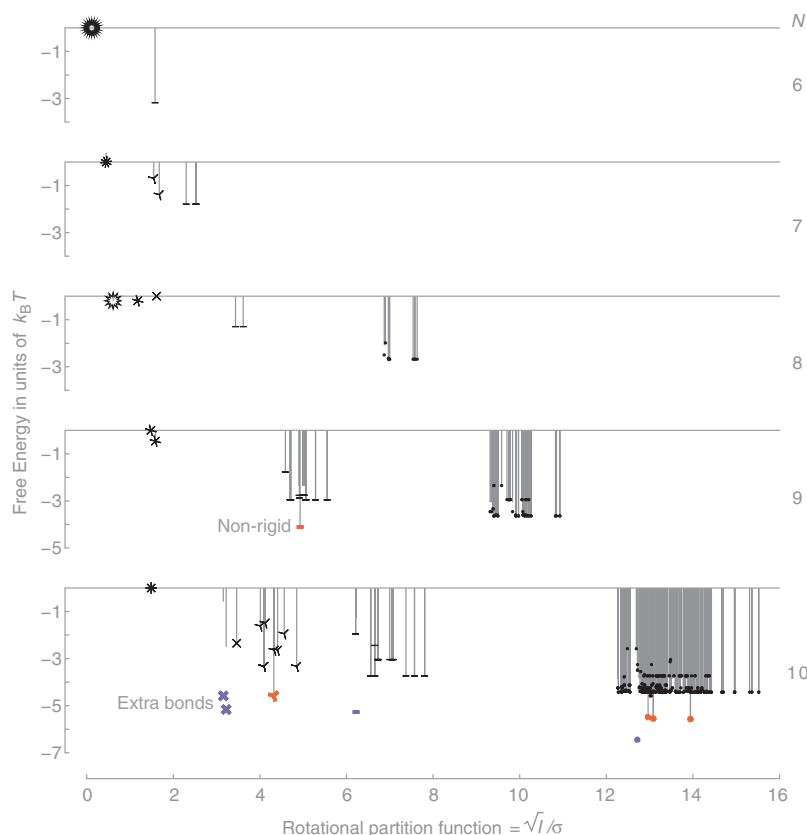


Fig. 4. Calculated minima of the free-energy landscape for $6 \leq N \leq 10$ (14). The x axis is in units of the rotational partition function, where I is the moment of inertia (calculated for a particle mass equal to 1) and σ is the rotational symmetry number. The bond strength for the calculation is $U_m = 4k_B T$. Each black symbol represents the free energy of an individual cluster. The number of spokes in each symbol indicates the symmetry number (dot = 1, line segment = 2, and so on). Orange symbols are nonrigid structures, which first appear at $N = 9$, and violet symbols have extra bonds, first appearing at $N = 10$. Vertical gray lines indicate the contribution to the free energy due to rotational and vibrational entropy. The reference states are chosen to be the highest free-energy states at each value of N . The general trend is for low-symmetry states to be favored in proportion to their rotational entropy, $k_B \ln(\sqrt{I}/\sigma)$. The potential-energy contribution accounts for the vertical space between the violet symbols and their gray lines.

energy, and therefore the rotational entropy selects against symmetric structures at all temperatures. Specifically, the symmetry number and the permutational degeneracy have the greatest effect on the free energy; differences in moment of inertia do not contribute as much. Thus, even if cluster rotations are hindered, as they may be in a bulk supercooled liquid, the permutational degeneracy might still influence the probability of formation. At higher N , the most probable structures we observe involve combinations of octahedra and tetrahedra. Many of these structures are compatible with an HCP lattice, but not with FCC. Our results also suggest that the curvature of the pair potential near the minimum should affect nucleation, because the curvature determines the free energy of the nonrigid clusters.

Structures with fivefold symmetry, such as the pentagonal dipyrmaid and icosahedron, are highly unfavorable in our system. Therefore we do not expect icosahedra or other clusters with

fivefold symmetry to be a structural motif in attractive hard-sphere gels or fluid cluster phases (26), where the attraction is short-ranged.

We find that the most stable small clusters of hard spheres with short-ranged attractions can be determined by geometrical rules: (1) rotational entropy favors structures with fewer symmetry elements; (2) vibrational entropy favors nonrigid clusters, which have half-octahedral substructures sharing at least one vertex; and (3) potential energy favors clusters with both octahedral and tetrahedral substructures, allowing them to have extra bonds.

Our picture of the free-energy landscape is still incomplete. The qualitative features of the landscape are independent of temperature for our experimental system because the depletion interaction is fundamentally entropic (14). This will not be the case for other types of interactions, such as DNA-mediated attractions (27). Also, under nonequilibrium conditions, we expect a different distribution of structures than the ones

shown here. Finally, our model for the landscape does not account for energy barriers or the connectivity between minima. It will be interesting to see if further studies can explain the emergence of bulk crystallization or structural arrest in terms of these topographical features and their geometrical underpinnings.

References and Notes

1. F. C. Frank, *Proc. R. Soc. Lond. A Math. Phys. Sci.* **215**, 43 (1952).
2. F. H. Stillinger, T. A. Weber, *Science* **225**, 983 (1984).
3. D. Nelson, F. Spaepen, *Solid State Phys.* **42**, 1 (1989).
4. J. P. K. Doye, D. J. Wales, *Science* **271**, 484 (1996).
5. H. Reichert *et al.*, *Nature* **408**, 839 (2000).
6. H. W. Sheng, W. K. Luo, F. M. Alamgir, J. M. Bai, E. Ma, *Nature* **439**, 419 (2006).
7. C. Patrick Royall, S. R. Williams, T. Ohtsuka, H. Tanaka, *Nat. Mater.* **7**, 556 (2008).
8. M. Hoare, P. Pal, *Adv. Phys.* **24**, 645 (1975).
9. M. Hoare, J. McInnes, *Adv. Phys.* **32**, 791 (1983).
10. D. J. Wales *et al.*, Cambridge Cluster Database, www-wales.ch.cam.ac.uk/CCD.html (2008).
11. D. J. Wales, T. V. Bogdan, *J. Phys. Chem. B* **110**, 20765 (2006).
12. J. P. K. Doye, F. Calvo, *J. Chem. Phys.* **116**, 8307 (2002).
13. R. L. Johnston, *Atomic and Molecular Clusters* (Taylor & Francis, New York, 2002).
14. Materials and methods are available as supporting material on Science Online.
15. V. J. Anderson, H. N. Lekkerkerker, *Nature* **416**, 811 (2002).
16. N. Arkus, V. N. Manoharan, M. P. Brenner, *Phys. Rev. Lett.* **103**, 118303 (2009).
17. M. Hoare, P. Pal, *Adv. Phys.* **20**, 161 (1971).
18. C. L. Brooks 3rd, J. N. Onuchic, D. J. Wales, *Science* **293**, 612 (2001).
19. K. A. Dill, H. S. Chan, *Nat. Struct. Biol.* **4**, 10 (1997).
20. Our particles are macroscopic and therefore distinguishable in principle. But we do not distinguish the particles in either the octahedral or polytetrahedral macrostate. The rotational partition function is therefore exactly the same as if we were to assume the particles to be indistinguishable.
21. G. Franke, E. R. Hilf, P. Borrmann, *J. Chem. Phys.* **98**, 3496 (1993).
22. J. Doye, D. Wales, *J. Chem. Soc., Faraday Trans.* **93**, 4233 (1997).
23. N. Johnson, *Can. J. Math.* **18**, 169 (1966).
24. J. Bernal, *Nature* **185**, 68 (1960).
25. V. N. Manoharan, M. T. Elsesser, D. J. Pine, *Science* **301**, 483 (2003).
26. A. Stradner *et al.*, *Nature* **432**, 492 (2004).
27. P. L. Biancaniello, A. J. Kim, J. C. Crocker, *Phys. Rev. Lett.* **94**, 058302 (2005).
28. S. Asakura, F. Oosawa, *J. Chem. Phys.* **22**, 1255 (1954).
29. A. Vrij, *Pure Appl. Chem.* **48**, 471 (1976).
30. We thank F. Spaepen and Z. Cheng for helpful discussions. We acknowledge support from NSF under award numbers DMR-0820484, CBET-0747625, and DMS-0907985; from the Defense Advanced Research Projects Agency under contract BAA 07-21; and from the Kavli Institute for Bionano Science and Technology at Harvard University.

Supporting Online Material

www.sciencemag.org/cgi/content/full/327/5965/560/DC1
Materials and Methods
Figs. S1 and S2
Tables S1 and S2
Movies S1 to S9

28 August 2009; accepted 10 December 2009
10.1126/science.1181263